Science Advances

AAAS

Supplementary Materials for

A general approach to composites containing nonmetallic fillers and liquid gallium

Chunhui Wang, Yan Gong, Benjamin V. Cunning*, Seunghwan Lee, Quan Le, Shalik R. Joshi, Onur Buyukcakir, Hanyang Zhang, Won Kyung Seong, Ming Huang, Meihui Wang, Jaeseon Lee, Gun-Ho Kim, Rodney S. Ruoff*

*Corresponding author. Email: rsruoff@ibs.re.kr, ruofflab@gmail.com (R.S.R.); ben.cunning@gmail.com (B.V.C.)
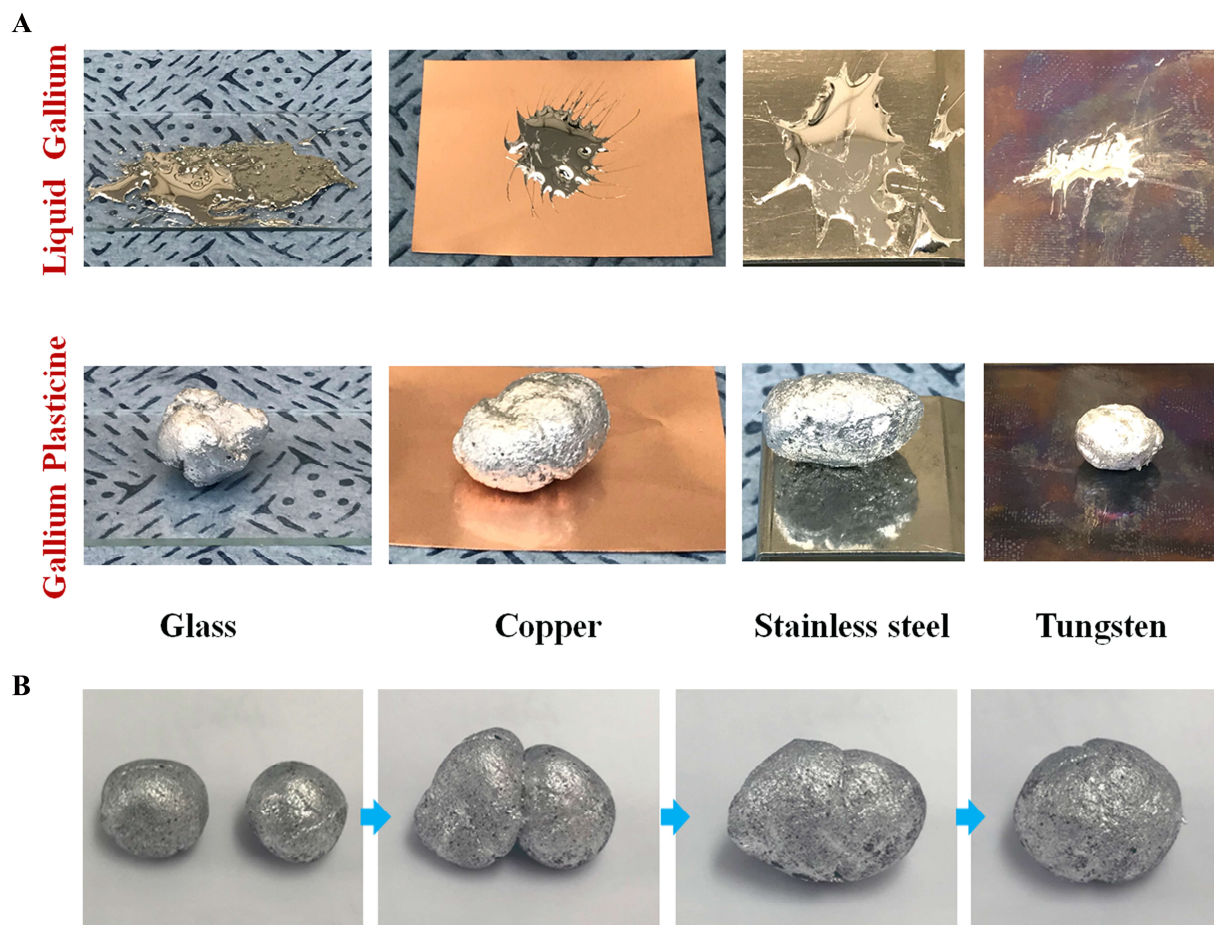
The PDF file includes:

Figs. S1 to S26
Tables S1 and S2
References

Other Supplementary Material for this manuscript includes the following:

(available at advances.sciencemag.org/cgi/content/full/7/1/eabe3767/DC1)

Movies S1 to S3

A

B

Figure S1. Photographs of Pure Ga and GalP (G-O) on various metal surfaces. (A) (top) Pure liquid gallium wets glass, copper, stainless steel, and tungsten, in air. Gallium is difficult to completely remove from the metal surface and grey stains of gallium oxide remain. (bottom) GalP (G-O) on the same metal surfaces. There is no wetting or stains visible on the surfaces. **(B)** Two pieces of GalP (G-O) can coalesce by bringing them into contact with gentle compression. This experiment was performed on a hotplate at 50 °C. This behavior was observed for all the GalPs tested, i.e. with rG-O, diamond, graphite, and silicon carbide.

The putty-like phase is a highly versatile form of Ga that would be ideal for manufacturing applications. In contrast to the liquid metal, GalP with incorporated G-O is cleaner to handle owing to its high cohesivity and non-staining properties. Grey stains of Ga oxide are usually left on substrates after processing liquid Ga, however this does not occur for all GalPs we synthesized. Clean macroscopic materials were easily prepared by common shaping methods including cutting, molding, and carving. Pieces of GalP can be joined together simply by bringing them into contact followed by gentle compression.
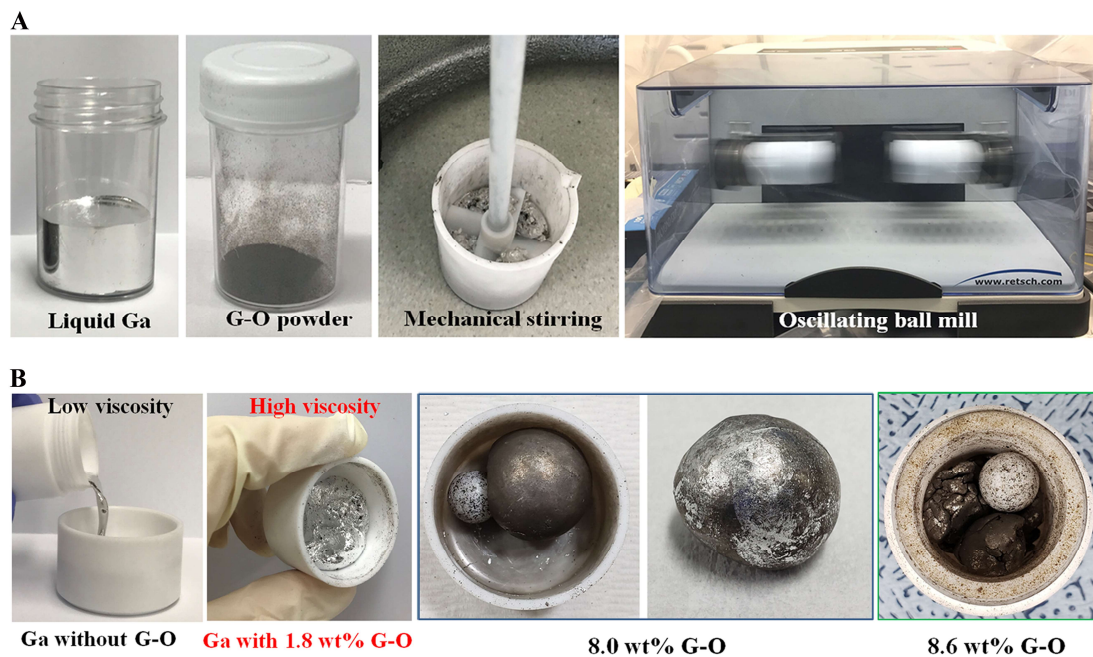
Figure S2. Photographs detailing the preparation of GalP (G-O) using plastic labware. (A) Pure liquid Ga and G-O powder stored in polyethylene containers. Mechanically stirred liquid gallium using Teflon components. An oscillating ball mill used after the mechanical stirring to incorporate additional G-O when the viscosity was too high for mechanical stirring. **(B)** Photos showing liquid Ga incorporated with different G-O loading masses; the maximum G-O loading is 8.0 wt %.

Because Ga wets silicate glass and readily forms alloys with most metals, we only used plastic labware in the preparation of GalP. In a typical experiment, 55.0 g of liquid Ga was added to a Teflon beaker by a plastic syringe or dropper and heated to 40 °C. Next, G-O powder was gradually added under mechanical stirring (we also attempted dispersion using sonication without success) and a putty-like phase was produced.

When the mass fraction of G-O exceeded 1.8 wt.%, the liquid turned into a highly viscous slurry. At this mass-fraction, the sample viscosity was too high for magnetic stirring to incorporate further G-O. Further incorporation of G-O could be achieved by transferring the mixture to an oscillating ball mill with additional G-O. The use of an oscillating ball mill allowed the addition of more G-O up to a maximum of 8.0 wt.%, but above 8.0 wt.% GalP (G-O) the material had a texture similar to partially dried clay. GalP (G-O) studied in this paper has a composition of 3.6 wt.%.
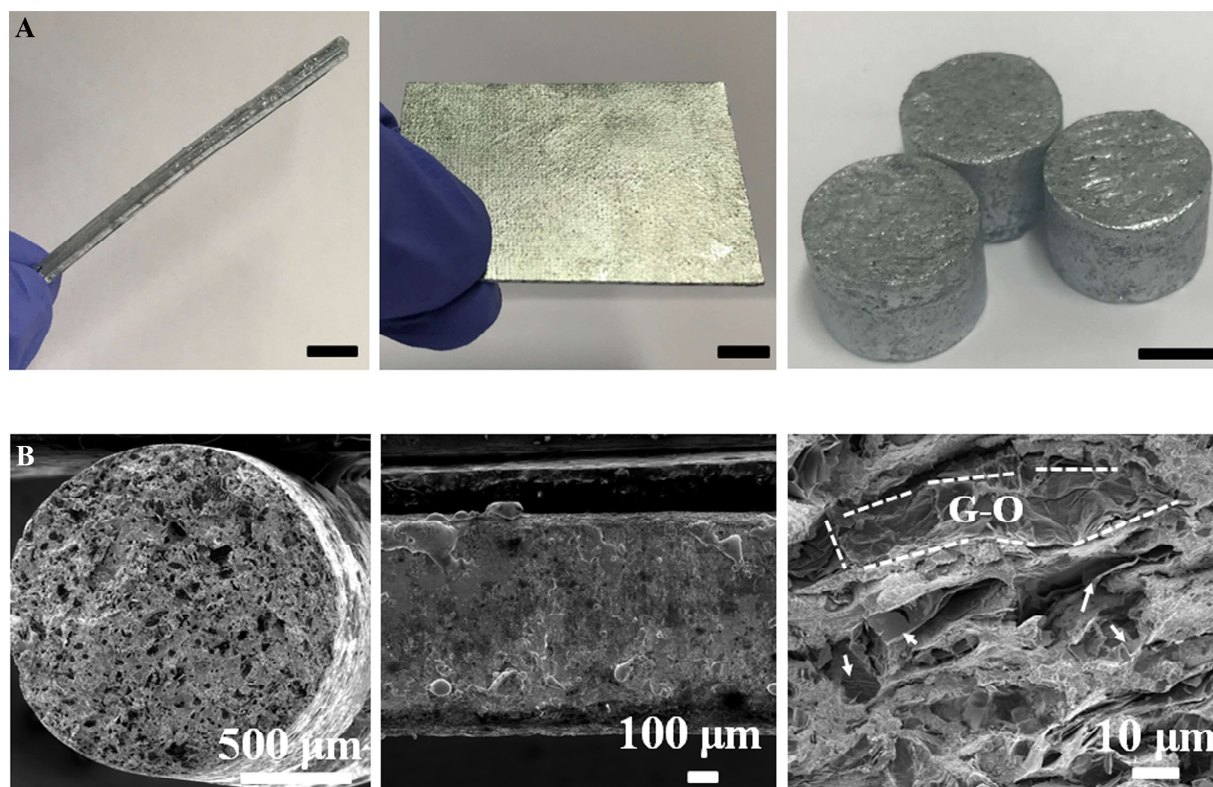
Figure S3. Customization of GalP (G-O) by molding. (A) A rod (or fiber), a plate (or film) and bulk blocks formed from GalP (G-O). All scale bars are 1 cm. **(B)** SEM images showing the cross sections of a rod and plate made from GalP (G-O) and a high-resolution SEM image resolving individual G-O sheets dispersed in the Ga.

GalP-based fibers and rods were made by injecting GalP (G-O) into Teflon tube molds. Plates or films could be easily peeled from substrates after the GalP (G-O) had solidified. The diameter and length of the samples could be changed over a large range by simply adjusting the mold size, which allows for the customization of GalP (G-O) for a broad range of applications. Bulk materials such as cylinders were prepared by filling correspondingly shaped molds with GalP (G-O).
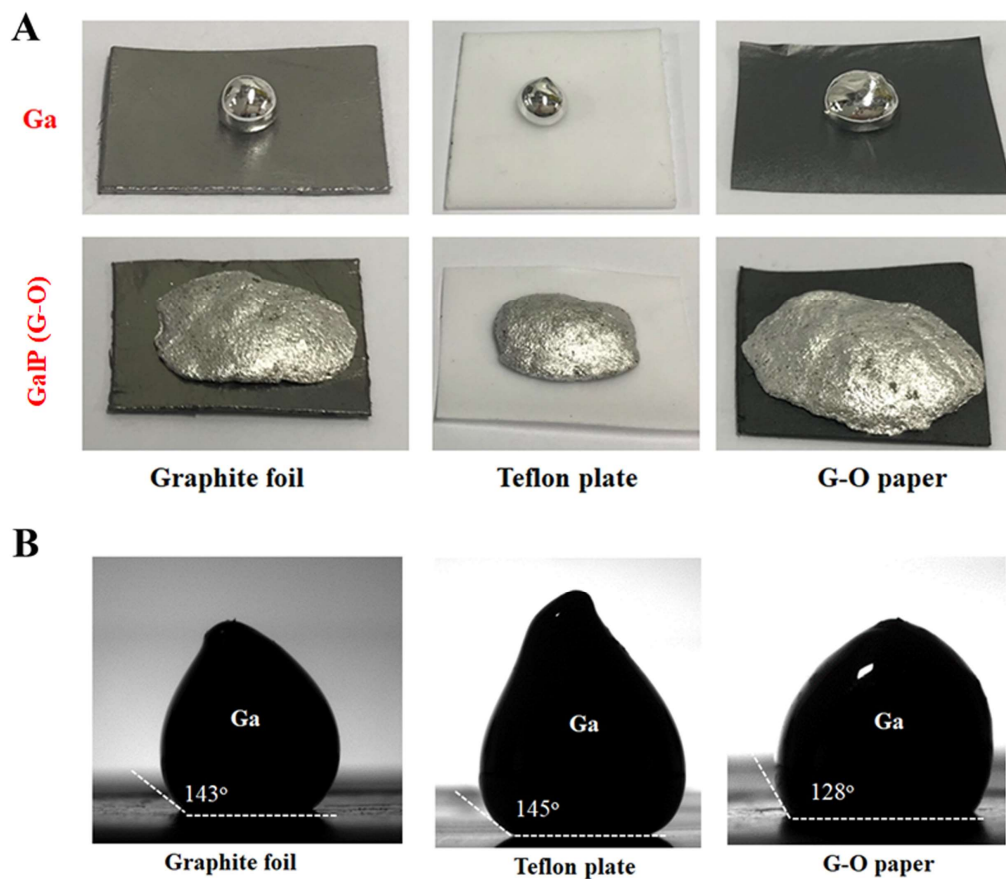
Figure S4. Photographs of Pure Ga and GalP (G-O) on various non-metallic substrates. (A) Liquid Ga usually forms globules on non-metallic substrates due to its high surface tension. In contrast, GalP (G-O) can readily spread on such substrates, e.g., graphite, Teflon, or graphene oxide. **(B)** The contact angles of pure Ga on graphite foil, a Teflon plate and G-O paper. Due to the favorable interaction between Ga oxide and G-O the contact angle on this substrate is lower. Measurements were performed at room temperature and Ga was a liquid during this experiment due to super cooling.
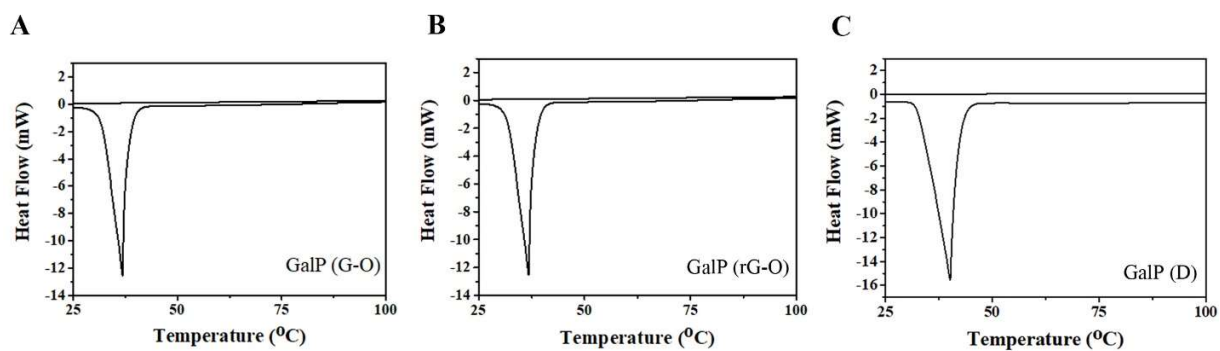
Figure S5. Differential scanning calorimetry (DSC) of GalP. (A) GalP (G-O), melting point: 31.9 °C. **(B)** GalP (rG-O), melting point: 32.1 °C, and **(C)** GalP (D), melting point: 32.3 °C.

Figure S6. Photographs showing the effect of freezing on both GalP (G-O) and pure Ga. (A) GalP (G-O) does not exhibit any volume change upon freezing and its molded shape is unchanged. **(B)** In contrast, the pure Ga forms a rounded top due to the high surface tension and expands during freezing, creating the 'spike' visible in the ingot (red circle).
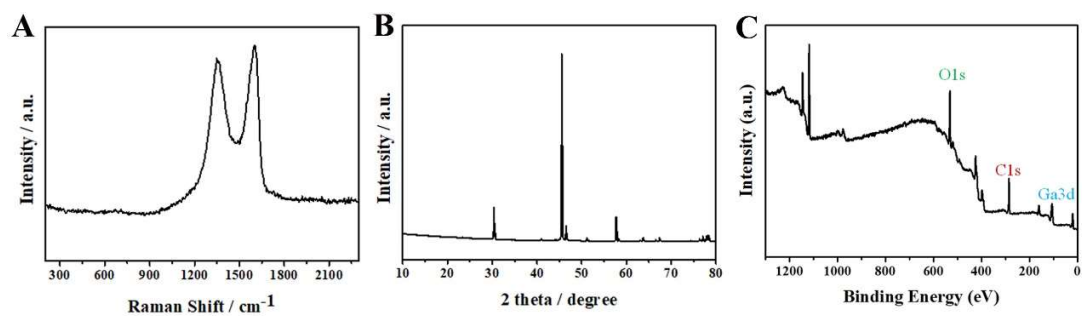
Figure S7. Chemical characterization of GalP (G-O). (A) Raman spectrum, **(B)** XRD pattern, and **(C)** XPS spectrum of the as-prepared GalP (G-O).

Raman spectroscopy of the GalP (G-O) showed two strong peaks at 1350 and 1598 cm^{-1}, corresponding to the D and G bands of G-O (Fig. S7A). The observed reflections in X-ray diffraction (XRD) matched the ICDD card no: 03-065-2493 for Ga (Fig. S7B). The chemical composition of the GalP (G-O) was investigated using X-ray photoelectron spectroscopy (XPS, Fig.S7C).
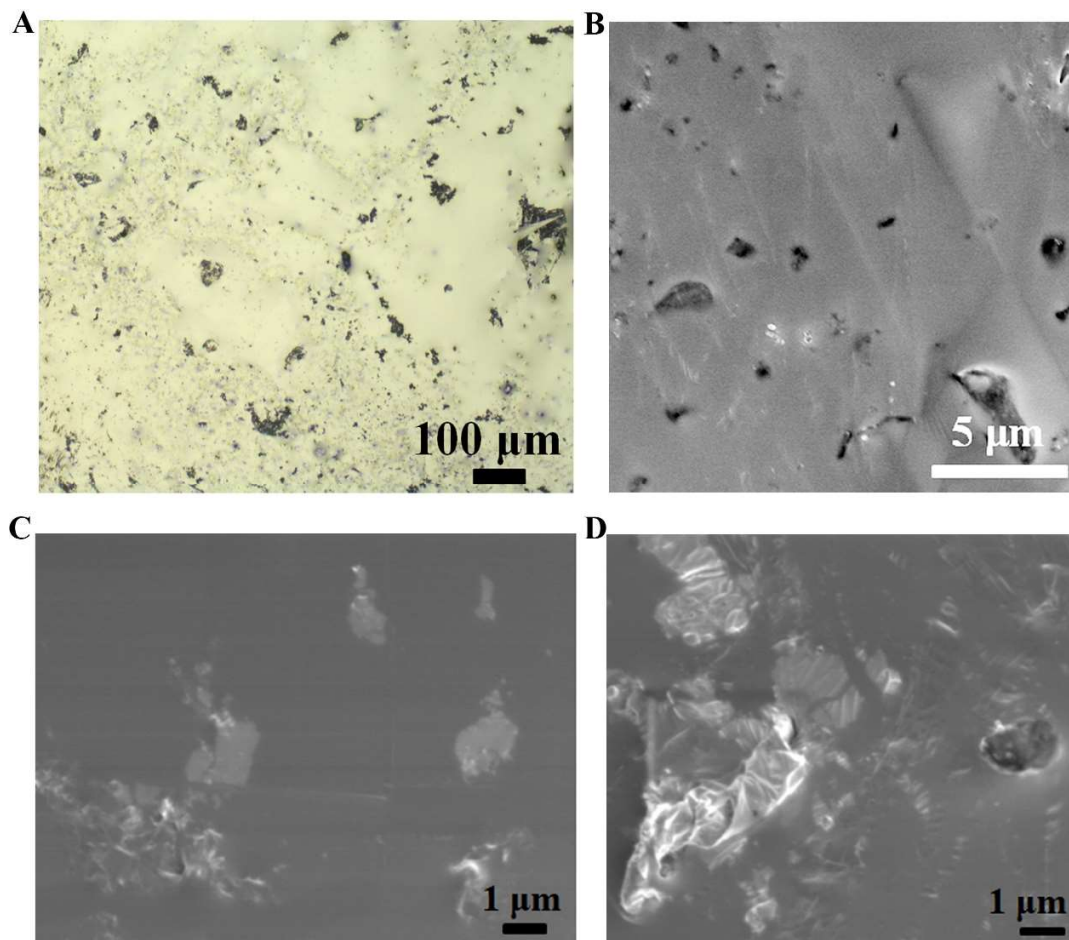
Figure S8. Optical microscope and SEM images of GaIP (G-O). (A) Optical microscope image of the GaIP (G-O). The black regions are due to the high optical absorption of G-O. **(B)** SEM image of the GaIP (G-O). **(C, D)** SEM images highlighting the aggregation of G-O when it is added to Ga; **(C)** A region with well-dispersed G-O in Ga and **(D)** a region with poorly dispersed G-O.
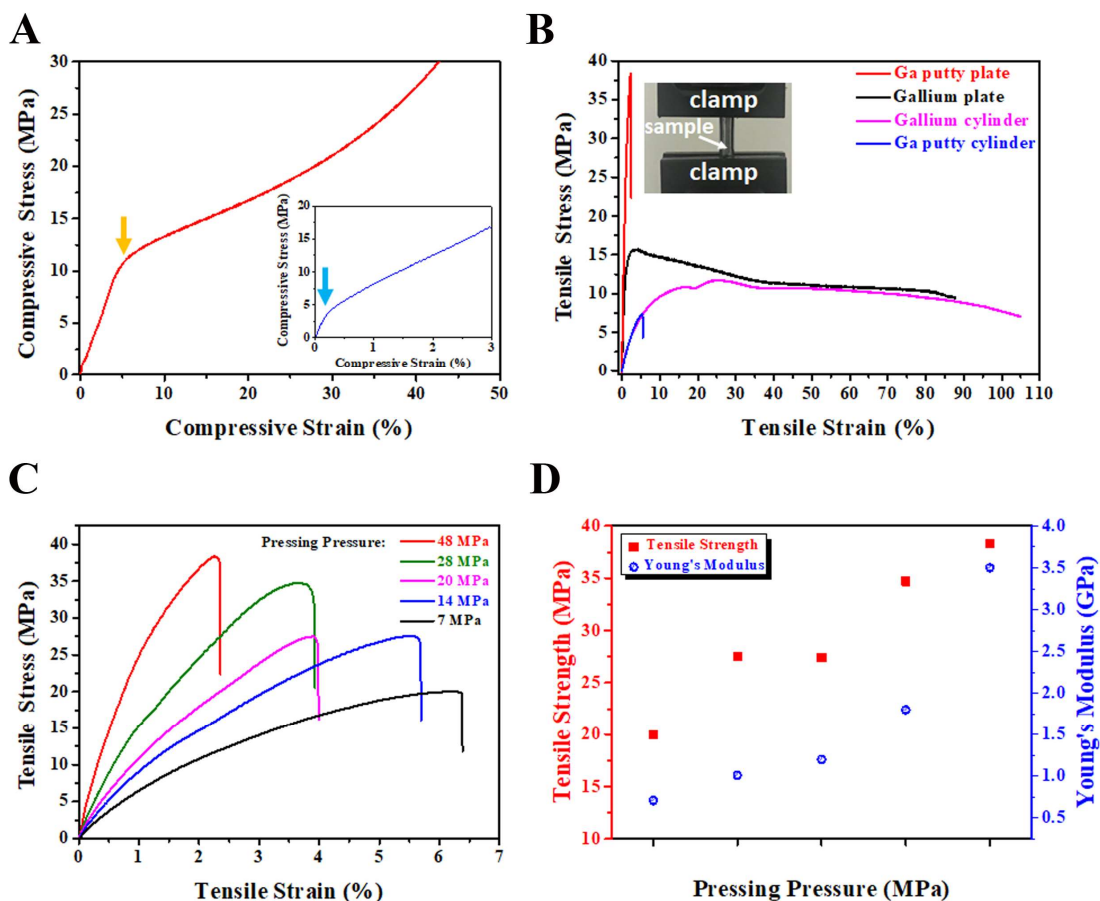
Figure S9. Mechanical strength of GaIP block, plate and rod. (A) Compressive test of a bulk GaIP (G-O) block. Inset: compressive test of a bulk pure Ga block. The arrows indicate the deformation of the samples. **(B)** Tensile testing of plates and cylinders made from pure Ga and GaIP (G-O). **(C)** Effect of cold pressing on the mechanical performance of an as-prepared GaIP (G-O) plate. **(D)** Comparison of tensile strength and Young's modulus of GaIP (G-O) plates pressed under different pressures.

The addition of G-O changed the mechanics relative to their pure Ga counterparts. As shown in Figure S9A, a pure Ga block deformed easily with a maximum compressive strength of 3.3 MPa, whereas the corresponding GaIP (G-O) block had a strength of 10.5 MPa, 3.2 times that of pure Ga.

Figure S9B compares the tensile strength of a GaIP (G-O) cylinder, a pure Ga cylinder, a GaIP (G-O) plate, and a pure Ga plate. Overall, the cylinders have larger fracture strains but lower strengths than the plates. This is due to the work hardening induced by pressing during the plate sample preparation. *(48)* It is also likely that pressing eliminated some of the voids and created a denser material. The tensile strength of the GaIP (G-O) plate is 38.3 MPa. It was possible to change the strength and fracture strain of our GaIP (G-O) plate by adjusting the compressive stress during pressing (Fig.S9C). Decreasing the pressing compressive stress from 48 MPa to 7 MPa, decreased the tensile strength of the GaIP (G-O) plate from 38.3 MPa to 19.8 MPa and the Young's modulus from 3.5 GPa to 0.7 GPa (Fig.S9D), while the fracture strain increased from 2.6% to 6.5%.

Figure S10. Photos showing how the particle size affects the incorporation. **(A)** silicon carbide, **(B)** diamond and **(C)** graphite into liquid Ga. When the particle size is large, a non-metallic particle is able to mix with Ga to form a putty-like composite.
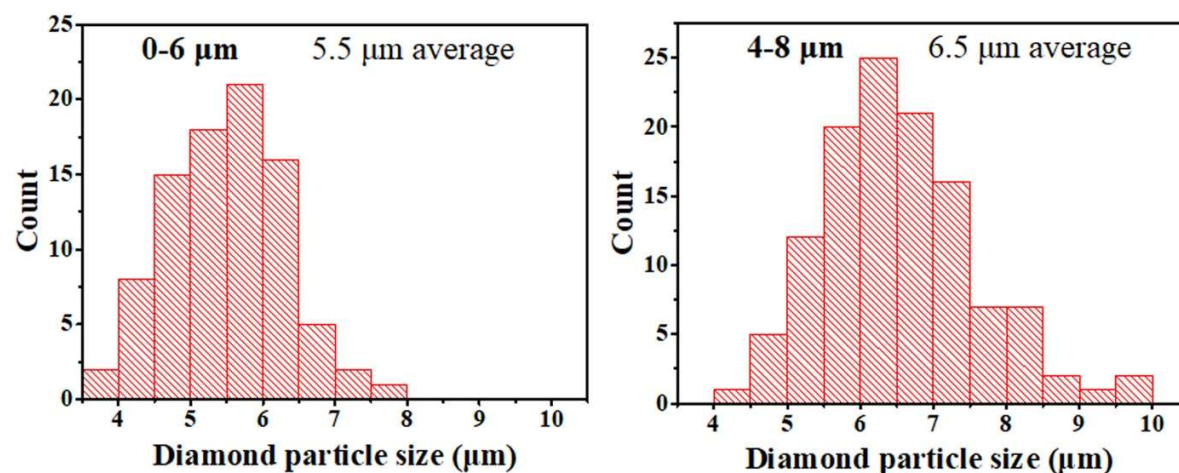
A

Diamond Particle Size	0.5 µm	0-6 µm	4-8 µm	8-15 µm
Result	Non-mixable	Non-mixable	mixable	mixable

Diamond Particle Size	10-20 µm	12-30 µm	30-40 µm	> 40 µm
Result	mixable	mixable	mixable	mixable

B

Figure S11. The mixability of synthetic diamond powders with varying particle sizes (Diamond Technologies, Thailand) in liquid Ga. (A) Particle size ranges are as reported by the manufacturer. The 0-6 µm range product was non-mixable but the 4-8 µm range product was mixable. **(B)** Measured size distribution (N≈100, optical microscopy) of diamond particles for the advertised 0-6 µm and 4-8 µm diamond particles.
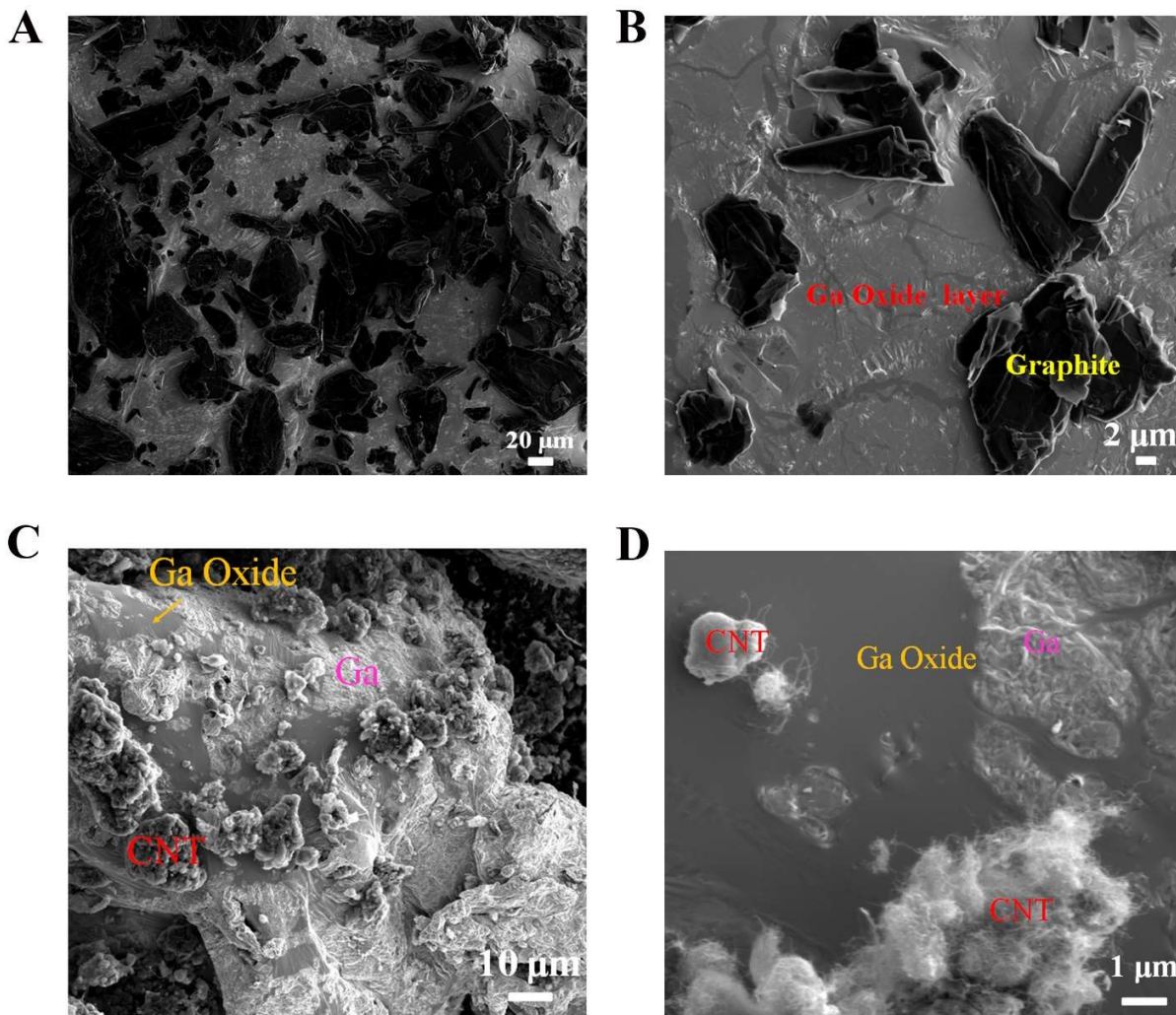
Figure S12. SEM images showing how the small particles are wrapped by Ga oxide and form a separate phase on Ga surface. (A, B) graphite (77 μm, average lateral size), **(C, D)** carbon nanotubes (multi-walled, 10 μm, average length).

We attempted to prepare GaIP by mixing liquid Ga with carbon nanotubes (CNTs, multi-walled, 2-20 μm, Sigma-Aldrich). However, these CNTs were 'non-mixable' and most CNTs were wrapped by the Ga oxide layer and floated on the surface of liquid Ga, resulting in two separate phases after mixing. The high curvature of CNTs impart a large effective roughness, and we have found that they bundle and entangle, further increasing the surface roughness and inhibiting mixing.
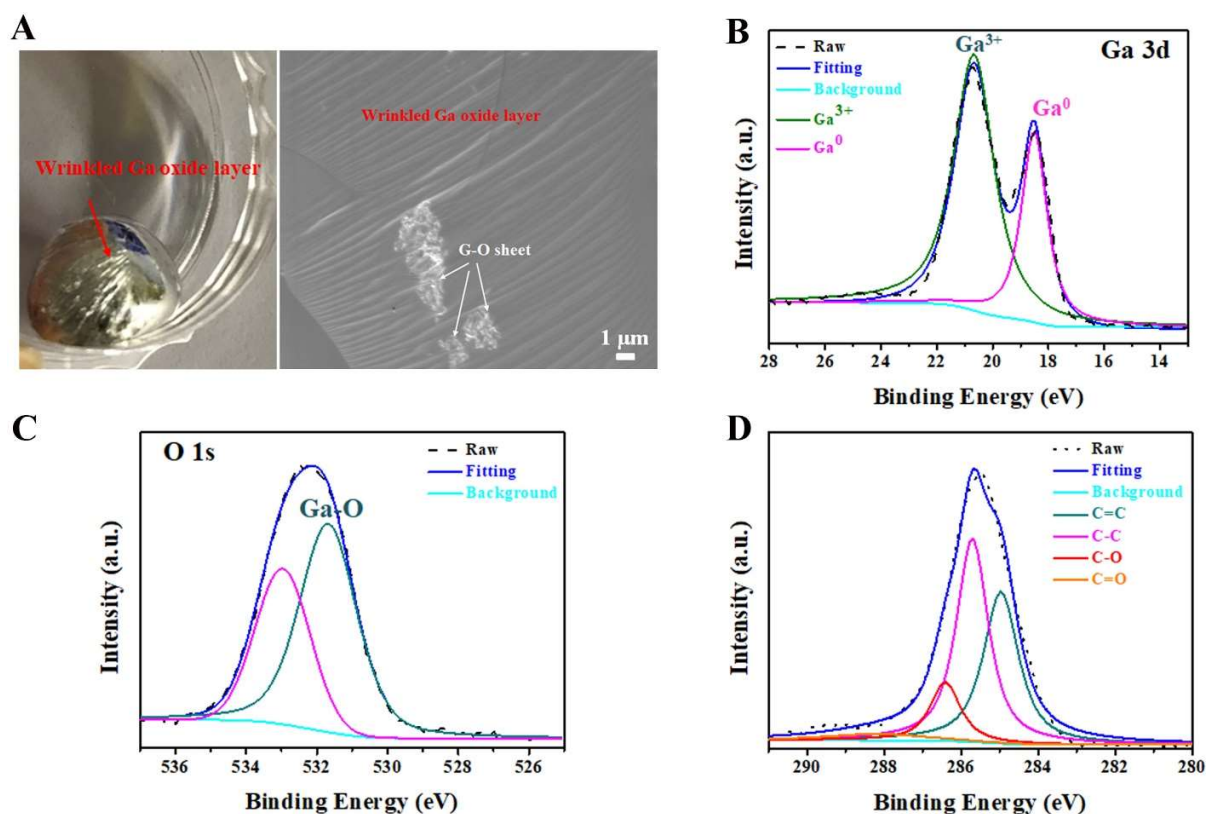
Figure S13. XPS spectra of a Ga oxide layer on the surface of a liquid Ga droplet. (A) (left) Photograph showing the presence of a thin gallium oxide skin on the surface of a liquid Ga droplet and (right) an SEM image showing the presence of the gallium oxide which appears wrinkled under electron imaging. In this image 3 G-O sheets are attached to the oxide layer. B-D) XPS spectra from the surface of the GaIP (G-O): **(B)** Ga 3d region **(C)** O 1s region, and **(D)** C 1s region.

SEM (Fig. S13A) was also used to evaluate the possible presence of Ga_2O_3 regions because oxidized regions have been reported to appear wrinkled or rippled *(49)*. In the Ga 3d XPS spectrum (Fig. S13B), the peak at 18.6 eV corresponds to metallic gallium (Ga^0), and the peak at 20.7 eV is due to the Ga^{3+} valence state in Ga_2O_3 *(50)*. The O 1s spectrum (Fig. S13C) was deconvoluted into two peaks, a high intensity peak centered at 531.7 eV and a low intensity peak at 533.5 eV. It has been reported that the O 1s peak in Ga-oxide occurs at ~531 eV, and is characteristic of the O bonding with the highest oxidation state of Ga (Ga^{3+}). The less intense contribution at ~533.5 eV is attributed to either carbonyl (oxygen bonded to carbon) or hydroxyl (oxygen bonded to hydrogen) groups *(5)*.The C 1s spectrum (Fig. S13D) shows four peaks at 284.6, 285.6, 286.9, and 288.2 eV corresponding to C=C, C-C, C-O, and C=O associated with the presence of G-O in the composite *(51)*.
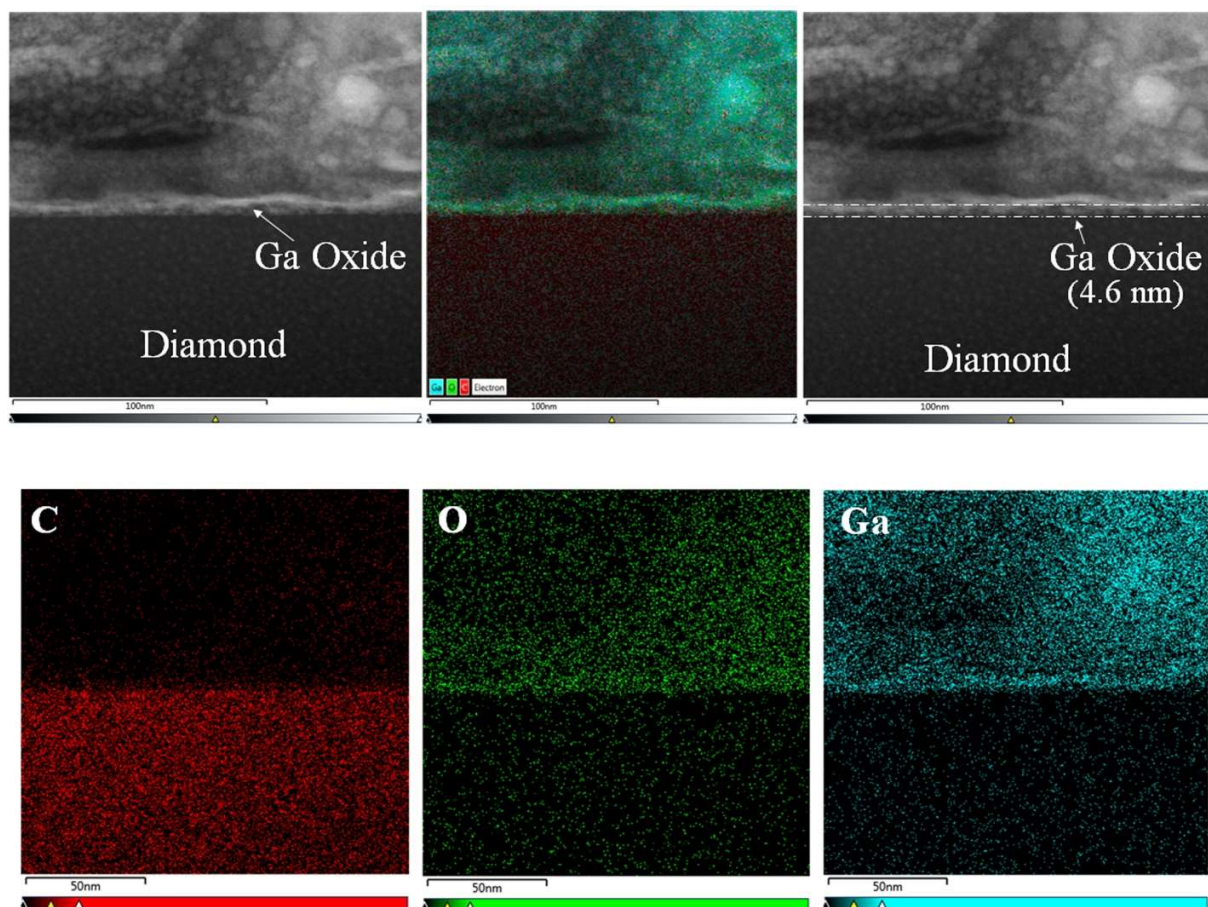
Figure S14. Scanning transmission electron microscope (STEM) images of GalP (D, ≈11 μm) with EDS elemental mapping showing the interface of the diamond particle and gallium. The dark field image shows the interfacial region between the bulk Ga and the diamond particle has a thin (≈4.6 nm) layer of bright contrast. STEM-EDS mapping of this region shows it has the highest concentration of oxygen, suggesting the particles are incorporated inside the Ga bulk wrapped by a gallium oxide skin. Specimens for these images were prepared by FIB.
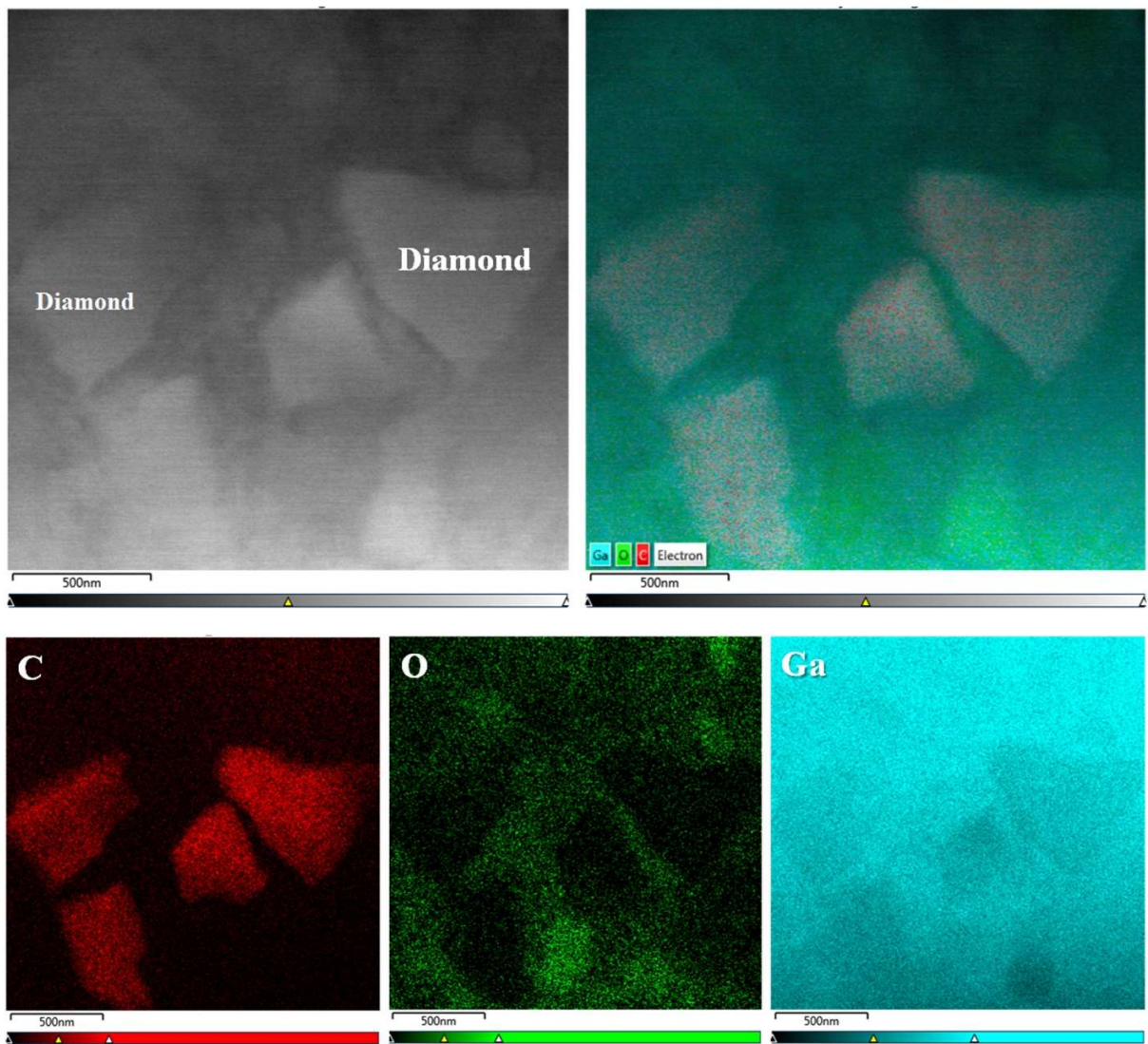
Figure S15. Lower magnification STEM images GaIP (D, ≈11 μm) with overlays of STEM-EDS elemental mapping. Specimens for these images were prepared by a dimpling grinder.
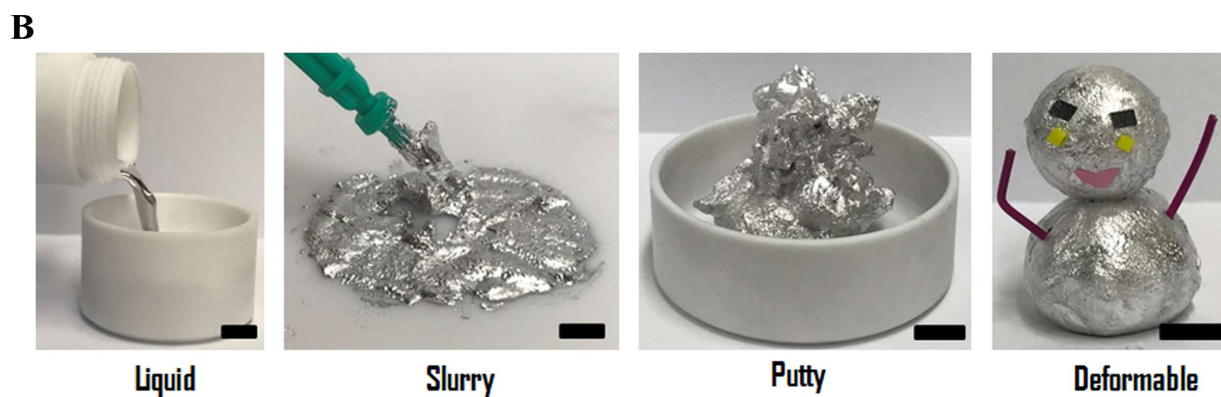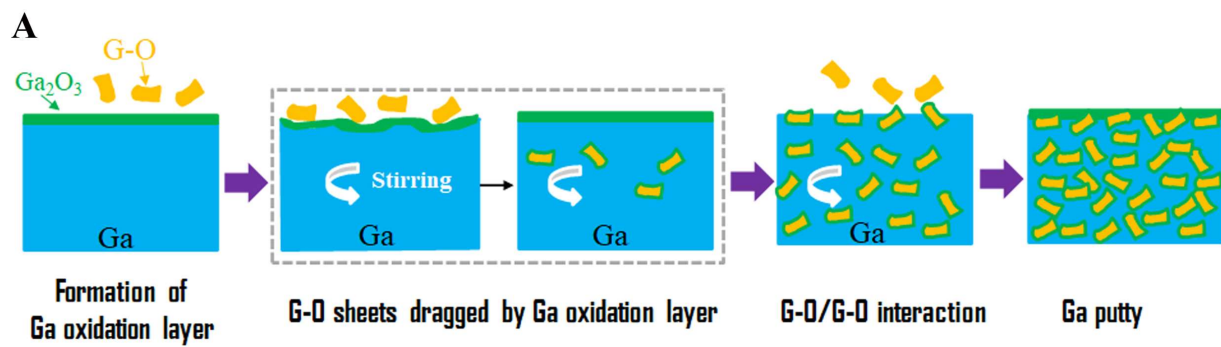
Figure S16. Illustration of the preparation of GaIP (G-O). (A) Schematic of the mechanism of the formation of GaIP (G-O). **(B)** Photos showing liquid gallium transitioning from a liquid to a thick slurry, and to a malleable putty. The metallic putty is highly processable and versatile, it can be molded into a variety of shapes.

A

Filler	Average Particle Size (μm)	Minimum mass loading to form a plasticine	Maximum mass loading to form a plasticine
Diamond	6.5	17.4 wt.%	32.2 wt.%
Diamond	11.0	19.4 wt.%	34.5 wt.%
Diamond	18.5	21.8 wt.%	39.5 wt.%
Diamond	35.6	22.4 wt.%	40.0 wt.%
Diamond	155	27.6 wt.%	41.9 wt.%
Silicon Carbide	102	27.3 wt.%	35.7 wt.%
Graphite	180	31.2 wt.%	32.5 wt.%
Graphene Oxide	12	1.8 wt.%	8.0 wt.%

B

Low volume loading	High volume loading	Deformable GalP
Ga behavior dominates	Ga_2O_3 behavior dominates	
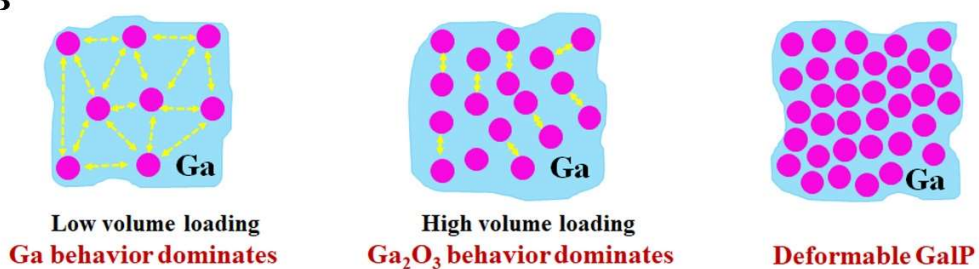
Figure S17. Effect of filler volume on the formation of GalP. (A) Estimated minimal and maximum filler loading for various particles to form the stable GalPs. **(B)** Illustration showing as the filler volume increases, gallium-skin behavior dominates and the GalP bulk is an interconnected network of liquid gallium and its associated oxide skin between filler particles.

Figure S18. Eutectic putty prepared by mixing G-O with EGaIn, EGaSn and Galinstan. The high malleability allows them to be kneaded to the "In", "Sn" and "IS" letters shown. All scale bars are 2 cm.

Eutectic gallium putties were prepared by mixing EGaIn, EGaSn, and Galinstan with G-O. We also attempted the same control experiment that we used for pure Ga; attempting to mix G-O with Ga eutectics in an inert and moisture free environment. As for pure Ga, they did not mix, indicating that the oxide layer is necessary for mixing. Based on prior studies (cited in main text), there is every reason to assume that gallium oxide formation at the surface of the 3 eutectics is similar to that for pure gallium, and then through the mixing process, this "skin" of gallium oxide is constantly mixed into the interior.
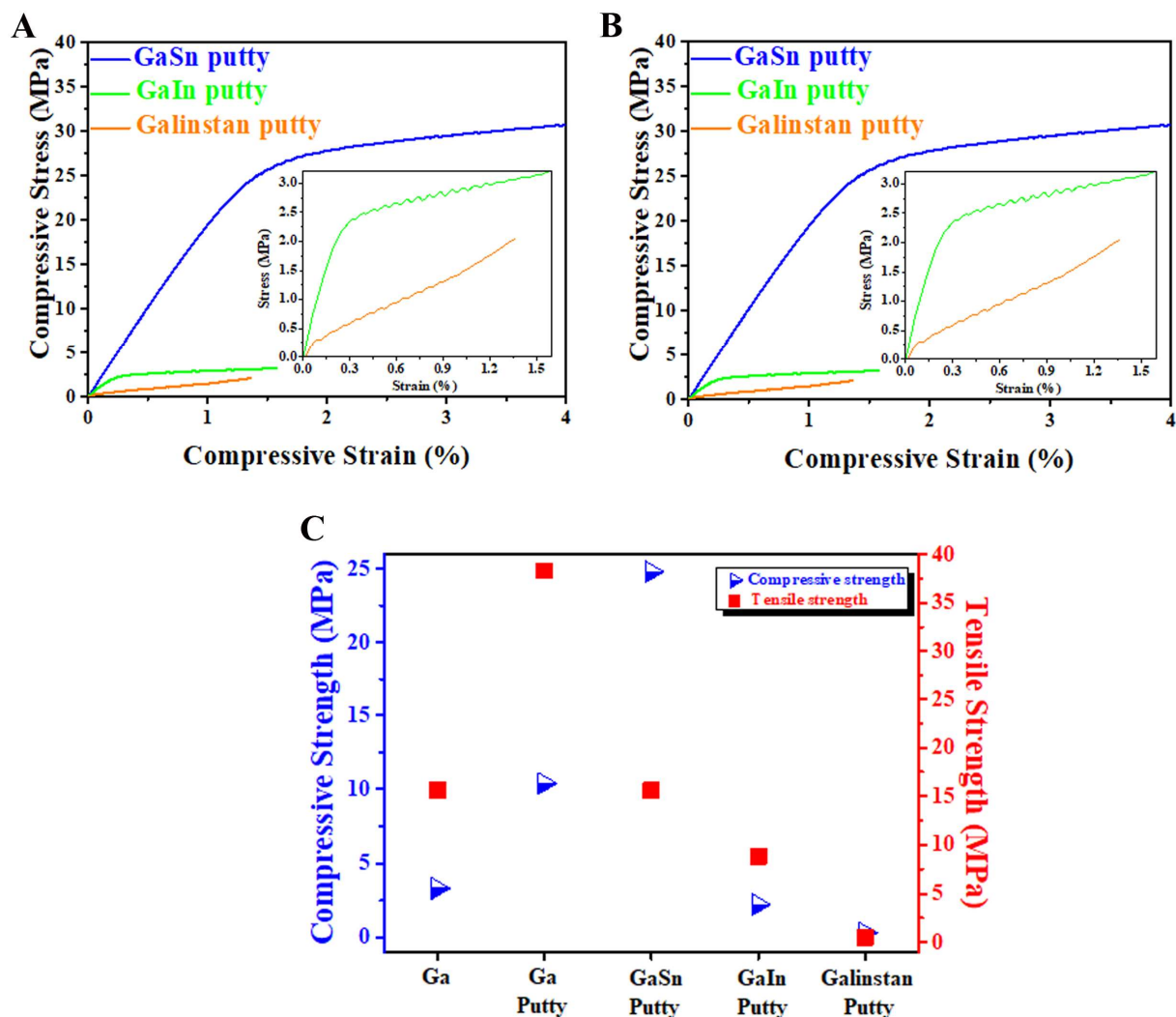
Figure S19. Mechanical strength of eutectic gallium putties. (A, B) Tensile and compressive stress-strain curves of "eutectic gallium putty" plates made from GaIn, GaSn and Galinstan putty and G-O. **(C)** Comparison of maximum compressive and tensile strengths of GLM putties made from G-O.

The eutectic gallium putties have a similar processability to GalP (G-O) and can be pressed into different shapes for different functions. We fabricated plates and cylinders from these putties by solidifying them at -80 °C and tested them at -50 to -40 °C. The EGaSn putty showed the best performance with a maximum compressive strength of 24.5 MPa and tensile strength of 15.7 MPa. The respective values for EGaIn are 8.6 MPa and 2.2 MPa and for Galinstan 0.5 MPa and 0.3 MPa.
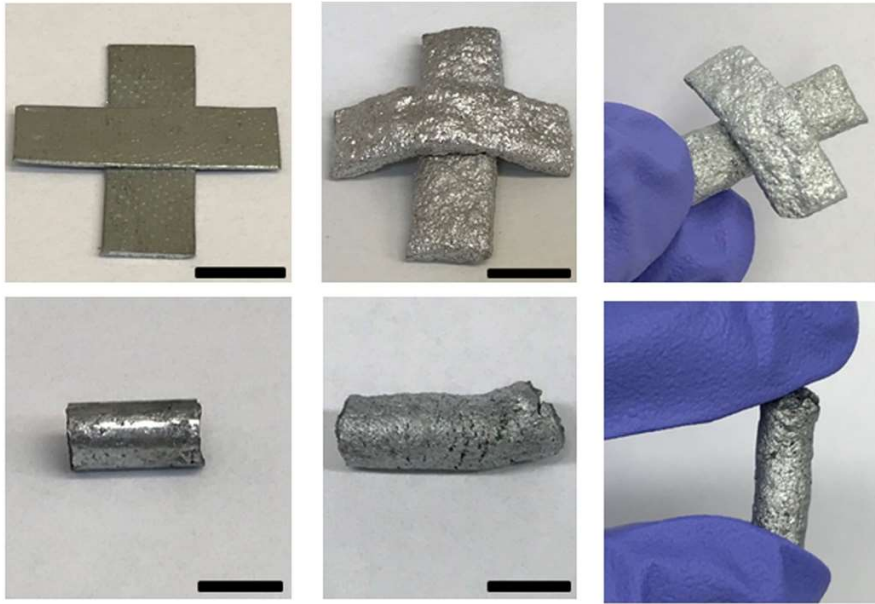
| GalP (G-O) putty | Heating | Ga/rG-O foam |

Figure S20 Photos showing the volume changes of GalP (G-O) putty plate and cylinder while being heated. (A) two GalP (G-O) plates. **(B)** a cylinder. All the scale bars are 2 cm.
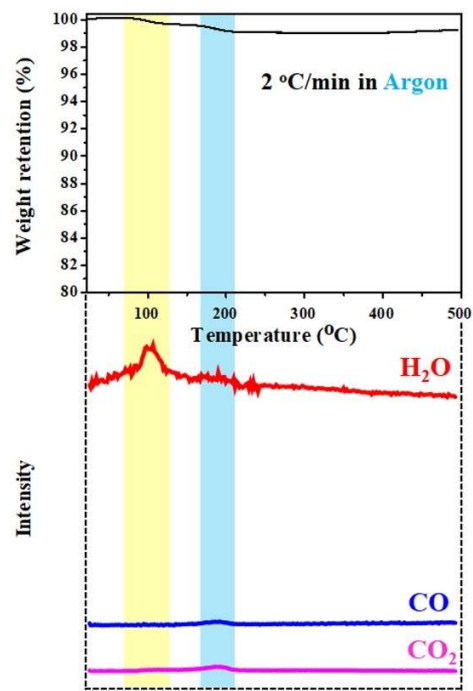
Figure S21. Thermogravimetric analysis coupled with mass spectrometry (TGA-MS) of GalP (G-O). The results show that the thermal expansion is caused by the release of water vapor, carbon monoxide, and carbon dioxide.
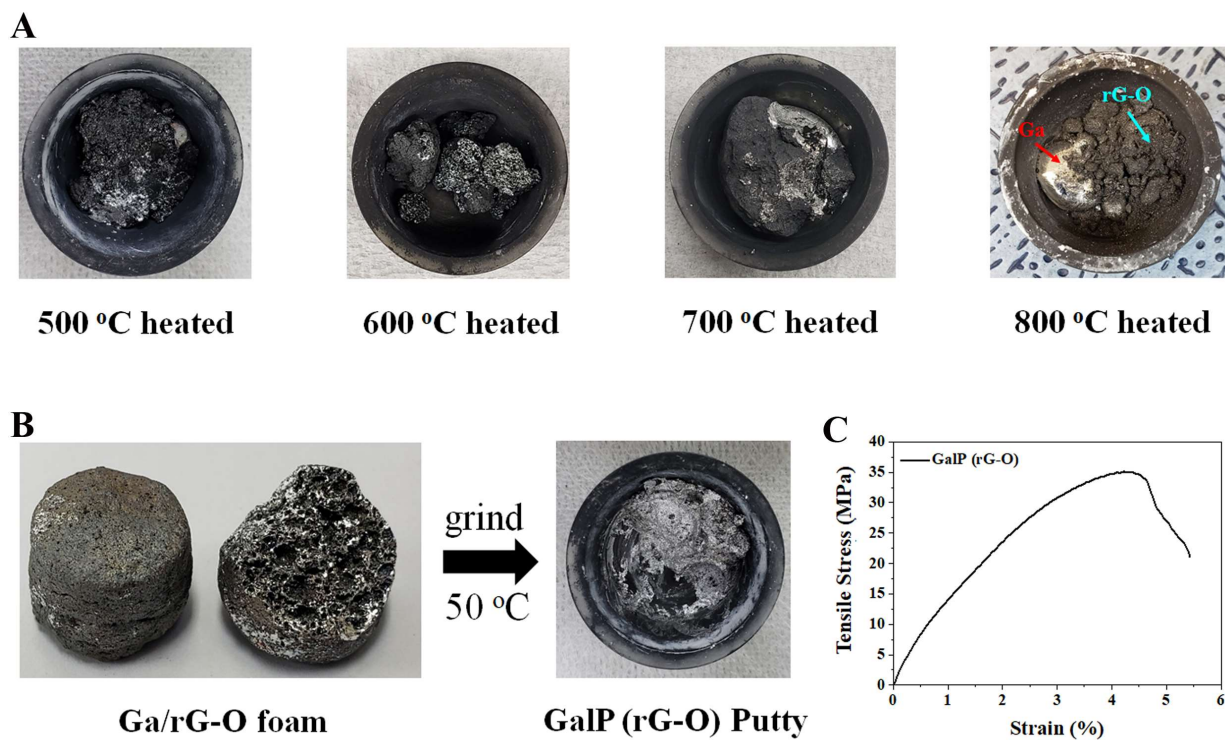
Figure S22. Optical photos showing a piece of GalP (G-O) was heated at different temperatures and a Ga/rG-O foam was turned into a putty by grinding. (A) A piece of GalP (G-O) without molding was heated at different temperatures under flowing Ar. The rG-O separated from Ga when the heating temperature was above 700 °C. **(B)** The Ga/rG-O foam can be ground to viscous GalP (rG-O) putty at elevated temperature. **(C)** Tensile stress-strain curves of GalP (rG-O) putty at room temperature.
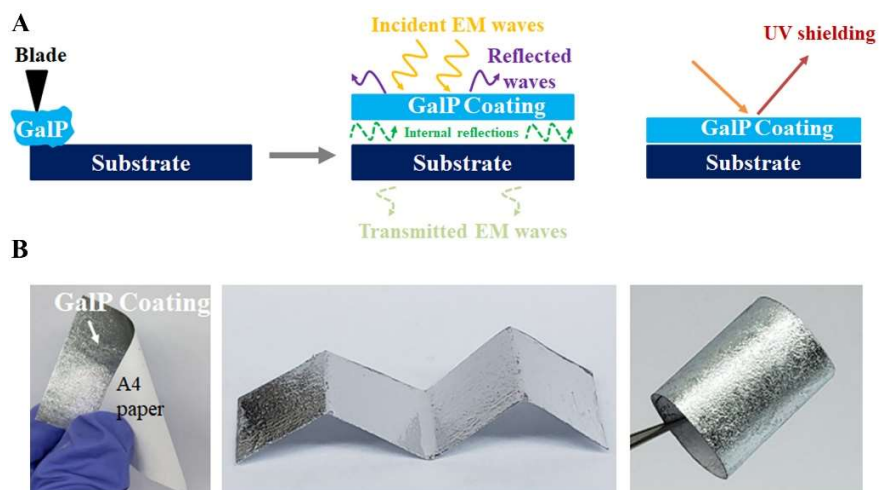
Figure S23. GalP (rG-O) putty used as an EMI and UV shielding coating. (A) Schematic of the mechanism of EMI and UV shielding by GalP (rG-O) coating. **(B)** Photos showing a piece of commercial A4 paper with GalP (rG-O) coating. The coated paper is flexible and it can be folded or rolled.
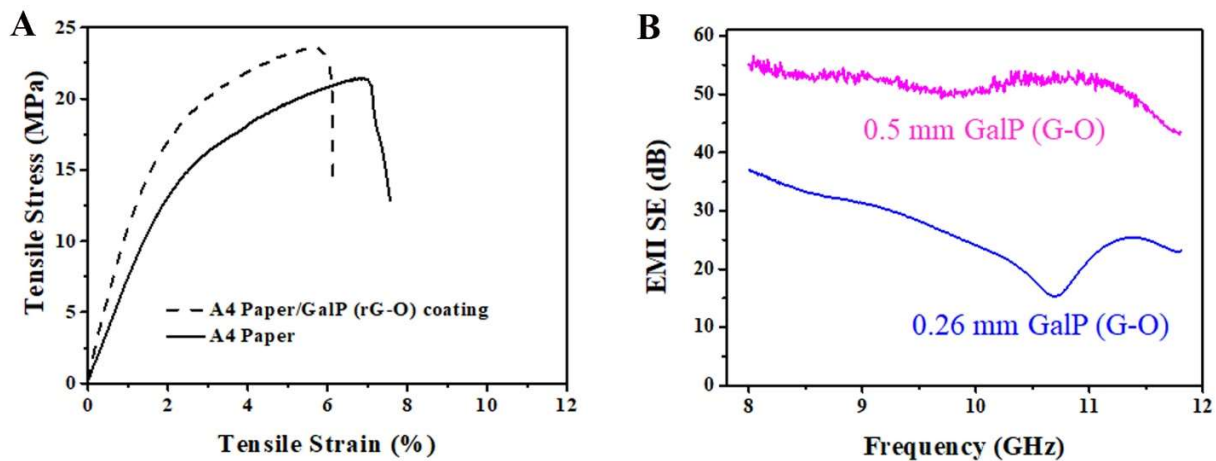
Figure S24. Tensile stress of a GalP (rG-O) coated A4 paper and EMI SE of GalP (G-O) with different thickness. **(A)** Stress-strain curves of A4 paper and A4 paper coated with a 10 μm-thick GalP (rG-O) coating; **(B)** EMI SE of GalP (G-O) with different thickness; compared with GalP (rG-O), the GalP (G-O) had a lower EMI SE because of the lower conductivity of G-O.
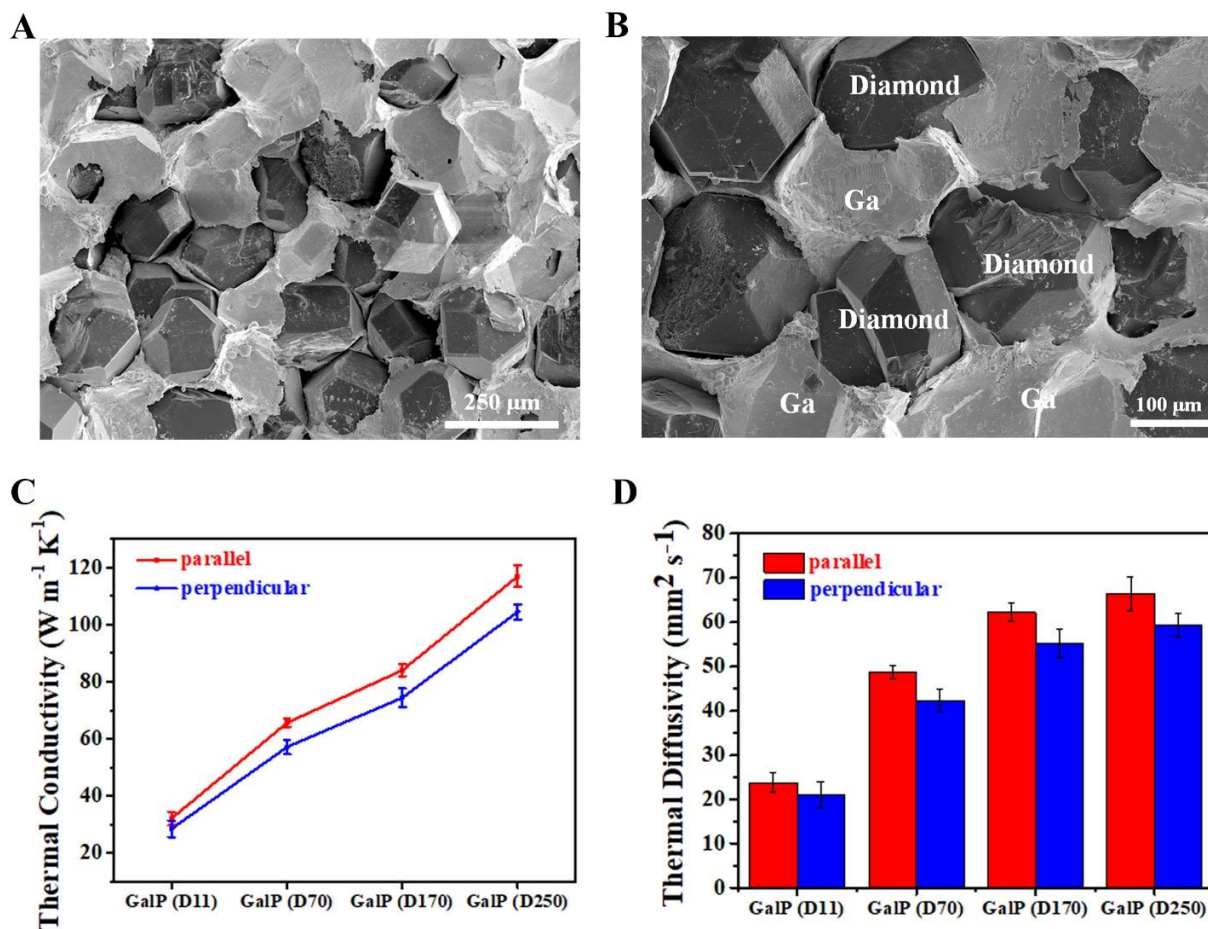
Figure S25. SEM images, thermal conductivities and diffusivities of GalP (D). (A, B) SEM images of GalP (D170 μm) at different magnifications; **(C, D)** Thermal conductivities and diffusivities of GalP (D) with different sized diamond particles. D11, D170, D250 and D250 represent diamond particle with average sizes of 11, 170, 250 and 250 μm, respectively.

The thermal conductivities of each sample are shown as below:

Sample	Parallel (W m⁻¹ K⁻¹)	Perpendicular (W m⁻¹ K⁻¹)
GalP (D11)	32.1±2.3	28.5±2.9
GalP (D70)	65.6±1.5	57.1±2.5
GalP (D170)	84.1±2.1	74.4±3.2
GalP (D250)	116.9±3.8	104.5±2.7
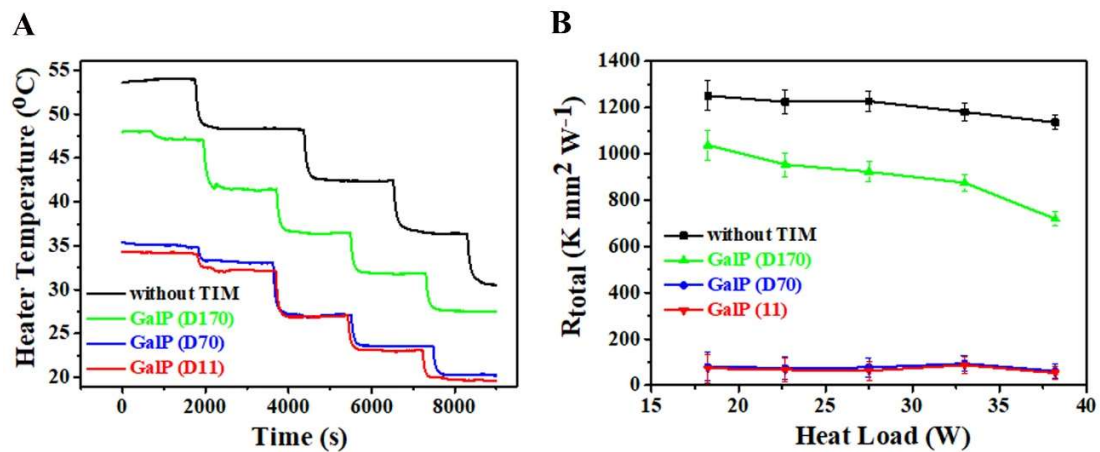
Figure S26. Temperature change of the stainless-steel heater as a function of the heating time and total thermal resistance of GalP (D) samples. (A) Temperature change of a heat source with attached heat sink (measured at the heat source) as a function of time with the TIM consisting of GalP (D) of varying particle sizes. Although GalP (D) with larger particle sizes show higher thermal conductivity and diffusivity (Figure S25), the larger particles protrude from the GalP (D) creating roughness and air gaps at the heat source – heat sink interface in turn decreasing performance as a TIM; **(B)** Total thermal resistance of GalP (D) samples.

Table S1. Comparison of EMI shielding performance for various materials.

Material	Thickness [mm]	EMI SE in X band [dB]	SSE [dB cm^3 g^{-1}]	SSEt [dB cm^2 g^{-1}]	Ref.
Cu foil	3.1	90	10	32	[52]
Ni foil	/	82	9.2	/	[52]
Stainless steel foil	4	89	11	28	[52]
Ag foil	0.01	58	5.6	5576	[53]
Al foil	0.05	63	23.2	4630	[53]
Graphene film	0.0084	20	/	/	[54]
Graphene/PEI foam	2.3	11	38	165	[55]
rGO/PU foam	2	20	663	3316	[56]
rGO/PI foam	0.8	21	75	937	[57]
rG-O/GalP (rG-O) film	**0.02**	**66**	**49.6**	**24812**	**This work**

Table S2. **Thermal conductivity of various commercial TIM materials.**

Brand name	Type	Thermal Conductance	Active Ingredient
IC Diamond ®	Grease Paste	4.5 W/mK	Micron Diamond
Thermaltake TG-8	Grease Paste	4.7 W/mk	Diamond powder
Thermal Grizzly Aeronaut	Grease Paste	8.5 W/mK	Metal particles
MasterGel Maker	Grease Paste	11 W/mk	Nano-diamond
PK-3 Thermal Compound	Grease Paste	11.2 W/mK	Nano Aluminum particles, ZnO
Thermal Grizzly KRYONAUT	Grease Paste	12 W/mK	Nano Aluminum particles, ZnO
Coollaboratory Liquid Copper	Grease Paste	12.5 W/mK	Matrix of silicone, micro-copper particles (99,9%)
Thermal Grizzly CONDUCTONAUT	Liquid	73 W/mK	Ga, In, Sn
Coollaboratory Liquid Extreme	Liquid	41 W/mK	100% liquid metal alloy
Coollaboratory Liquid Ultra	Liquid	38 W/mK	100% liquid metal alloy
Silver King	Liquid	79 W/mK	100% liquid metal alloy

REFERENCES AND NOTES

1. J. J. Yan, Y. Lu, G. J. Chen, M. Yang, Z. Gu, Advances in liquid metals for biomedical applications. *Chem. Soc. Rev.* **47**, 2518–2533 (2018).

2. T. Daeneke, K. Khoshmanesh, N. Mahmood, I. A. de Castro, D. Esrafilzadeh, S. J. Barro, M. D. Dickey, K. Kalantar-zadeh, Liquid metals: Fundamentals and applications in chemistry. *Chem. Soc. Rev.* **47**, 4073–4111 (2018).

3. K. Kalantar-Zadeh, J. B. Tang, T. Daeneke, A. P. O'Mullane, L. A. Stewart, J. Liu, C. Majidi, R. S. Ruoff, P. S. Weiss, M. D. Dickey, Emergence of liquid metals in nanotechnology. *ACS Nano* **13**, 7388–7395 (2019).

4. Q. Wang, Y. Yu, J. Liu, Preparations, characteristics and applications of the functional liquid metal materials. *Adv. Eng. Mater.* **20**, 1700781(2018).

5. M. D. Dickey, R. C. Chiechi, R. J. Larsen, E. A. Weiss, D. A.Weitz, G. M. Whitesides, Eutectic gallium-indium (EGaIn): A liquid metal alloy for the formation of stable structures in microchannels at room temperature. *Adv. Funct. Mater.* **18**, 1097–1104 (2008).

6. M. F. Dumke, T. A. Tombrello, R. A. Weller, R. M. Housley, E. H. Cirlin, Sputtering of the gallium-indium eutectic alloy in the liquid phase. *Surf. Sci.* **124**, 407–422 (1983).

7. T. Liu, P. Sen, C. C. J. Kim, Characterization of nontoxic liquid-metal alloy galinstan for applications in microdevices. *J. Microelectromech. Syst.* **21**, 443–450 (2012).

8. R. Guo, X. L. Wang, H. Chang, W. Z. Yu, S. T. Liang, W. Rao, J. Liu, Ni-GaIn amalgams enabled rapid and customizable fabrication of wearable and wireless healthcare electronics. *Adv. Eng. Mater.* **20**, 1800054 (2018).

9. C. F. Pan, E. J. Markvicka, M. H. Malakooti, J. J. Yan, L. M. Hu, K. Matyjaszewski, C. Majidi, A liquid-metal-elastomer nanocomposite for stretchable dielectric materials. *Adv. Mater.* **31**, 1900663 (2019).

10. S. Liu, M. C. Yuen, E. L. White, J. W. Boley, B. Deng, G. J. Cheng, R. Kramer-Bottiglio, Laser sintering of liquid metal nanoparticles for scalable manufacturing of soft and flexible electronics. *ACS Appl. Mater. Interfaces* **10**, 28232–28241 (2018).

11. X. K. Li, M. J. Li, L. Zong, X. C. Wu, J. You, P. K. Du, C. X. Li, Liquid metal droplets wrapped with polysaccharide microgel as biocompatible aqueous ink for flexible conductive devices. *Adv. Funct. Mater.* **28**, 1804197 (2018).

12. M. D. Bartlett, N. Kazem, M. J. Powell-Palm, X. N. Huang, W. H. Sun, J. A. Malen, C. Majidi, High thermal conductivity in soft elastomers with elongated liquid metal inclusions. *Proc. Natl. Acad. Sci. U.S.A.* **114**, 2143–2148 (2017).

13. I. D. Joshipura, H. R. Ayers, C. Majidi, M. D. Dickey, Methods to pattern liquid metals. *J. Mater. Chem. C* **3**, 3834 (2015).

14. W. Kong, Z. Y. Wang, M. Wang, K. C. Manning, A. Uppal, M. D. Green, R. Y. Wang, K. Rykaczewski, Oxide-mediated formation of chemically stable tungsten-liquid metal mixtures for enhanced thermal interfaces. *Adv. Mater.* **31**, 1904309 (2019).

15. J. Tang, X. Zhao, J. Li, R. Guo, Y. Zhou, J. Liu, Gallium-based liquid metal amalgams: Transitional-state metallic mixtures (TransM2ixes) with enhanced and tunable electrical, thermal, and mechanical properties. *ACS Appl. Mater. Interfaces* **9**, 35977–35987 (2017).

16. M. Tavakoli, M. H. Malakooti, H. Paisana, Y. Ohm, D. G. Marques, P. A. Lopes, A. P. Piedade, A. T. Almeida, C. Majidi, EGaIn-assisted room-temperature sintering of silver nanoparticles for stretchable, inkjet-printed, thin-film electronics. *Adv. Mater.* **30**, 1801852 (2018).

17. A. L. Lereu, F. Lemarchand, M. Zerra, M. Yazdanpanah, A. Passian, Optical properties and plasmonic response of silver-gallium nanostructures. *J. Appl. Phys.* **117**, 063110 (2015).

18. X. Wang, W. Yao, R. Guo, X. Yang, J. Tang, J. Zhang, W. P. Gao, V. Timchenko, J. Liu, Soft and moldable Mg-doped liquid metal for conformable skin tumor photothermal therapy. *Adv. Healthc. Mater.* **7**, 1800318 (2018).

19. X. Huang, X. Y. Qi, F. Boey, H. Zhang, Graphene-based composites. *Chem. Soc. Rev.* **41**, 666–686 (2012).

20. A. P. Yu, P. Ramesh, M. E. Itkis, E. Bekyarova, R. C. Haddon, Graphite nanoplatelet−epoxy composite thermal interface materials. *J. Phys. Chem. C* **111**, 7565–7569 (2007).

21. E. A. Ekimov, N. V. Suetin, A. F. Popovich, V. G. Ralchenko, Thermal conductivity of diamond composites sintered under high pressures. *Diam. Relat. Mater.* **17**, 838–843 (2008).

22. L. L. Snead, R. H. Jones, A. Kohyama, P. Fenici, Status of silicon carbide composites for fusion. *J. Nucl. Mater.* **233**, 26–36 (1996).

23. E. T. Thostenson, T. W. Chou, Processing-structure-multi-functional property relationship in carbon nanotube/epoxy composites. *Carbon* **44**, 3022–3029 (2006).

24. Y.-G. Park, H. Min, H. Kim, A. Zhexembekova, C. Y. Lee, J.-U. Park, Three-dimensional, high-resolution printing of carbon nanotube/liquid metal composites with mechanical and electrical reinforcement. *Nano Lett.* **19**, 4866–4872 (2019).

25. L. Y. Zhao, S. Chu, X. C. Chen, G. Chu, Efficient heat conducting liquid metal/CNT pads with thermal interface materials. *Bull. Mater. Sci.* **42**, 192 (2019).

26. V. Kamysbayev, N. M. James, A.S. Filatov, V. Srivastava, B. Anasori, H. M. Jaeger, Y. Gogotsi, D. V.Talapin, Colloidal gelation in liquid metals enables functional nanocomposites of 2D metal carbides (MXenes) and lightweight metals. *ACS Nano* **13**, 12415–12424 (2019).

27. S. Wei, Z. F. Yu, L. J. Zhou, J. D. Guo, Investigation on enhancing the thermal conductance of gallium-based thermal interface materials using chromium-coated diamond particles. *J. Mater. Sci. Mater. Electron.* **30**, 7194–7202 (2019).

28. B. Konkena, S. Vasudevan, Understanding aqueous dispersibility of graphene oxide and reduced graphene oxide through pKa measurements. *J. Phys. Chem. Lett.* **3**, 867–872 (2012).

29. İ. Mutlay, L. B. Tudoran, Percolation behavior of electrically conductive graphene nanoplatelets/polymer nanocomposites: Theory and experiment. *Fuller. Nanotub. Carbon Nanostructures*, **22**, 413–433 (2014).

30. A. Plech, U. Klemradt, H. Metzger, J. Peisl, In situ X-ray reflectivity study of the oxidation kinetics of liquid gallium and the liquid alloy $Ga_{0.93}Hg_{0.07}$. *J. Phys. Condens. Matter* **10**, 971–982 (1998).

31. M. D. Dickey, Emerging applications of liquid metals featuring surface oxides. *ACS Appl. Mater. Interfaces* **6**, 18369–18379 (2014).

32. J. Cutinho, B. S. Chang, S. Oyola-Reynoso, J. Chen, S. S. Akhter, I. D. Tevis, N. J. Bello, A. Martin, M. C. Foster, M. M. Thuo. Autonomous thermal-oxidative composition inversion and texture tuning of liquid metal surfaces. *ACS Nano* **12**, 4744–4753 (2018).

33. S. Liu, S. N. Reed, M. J. Higgins, M. S. Titus, R. Kramer-Bottiglio, Oxide rupture-induced conductivity in liquid metal nanoparticles by laser and thermal sintering. *Nanoscale* **11**, 17615–17629 (2019).

34. R. C. Chiechi, E. A. Weiss, M. D. Dickey, G. M. Whitesides, Eutectic gallium-indium (EGaIn): A moldable liquid metal for electrical characterization of self-assembled monolayers. *Angew. Chem. Int. Ed.* **47**, 142–144 (2008).

35. R. J. Larsen, M. D. Dickey, G. M. Whitesides, D. A. Weitz, Viscoelastic properties of oxide-coated liquid metals. *J. Rheol.* **53**, 1305–1326 (2009).

36. M. R. Khan, C. B. Eaker, E. F. Bowden, M. D. Dickey, Giant and switchable surface activity of liquid metal via surface oxidation. *Proc. Natl. Acad. Sci. U.S.A.* **30**, 14047–14051 (2014).

37. C. J. Zhang, Q. Yang, C. Shan, J. Z. Zhang, J. L. Yong, Y. Fang, X. Hou, F. Chen, Tuning a surface super-repellent to liquid metal by a femtosecond laser. *RSC Adv*. **10**, 3301–3306 (2020).

38. S. S. Kadlaskar, J. H. Yoo, Abhijeet, J. B. Lee, W. J. Choi, Cost-effective surface modification for Galinstan lyophobicity. *J. Colloid Interface Sci.* **492**, 33–40 (2017).

39. Z. Y. Chen, J. B. Lee, Surface modification with Gallium coating as nonwetting surfaces for Gallium-based liquid metal droplet manipulation. *ACS Appl. Mater. Interfaces* **11**, 35488–35495 (2019).

40. C. Ladd, J. H. So, J. Muth, M. D. Dickey, 3D printing of free standing liquid metal microstructures. *Adv. Mater.* **25**, 5081–5085 (2013).

41. A. R. Jacob, D. P. Parekh, M. D. Dickey, L. C. Hsiao, Interfacial rheology of gallium-based liquid metals. *Langmuir* **35**, 11774–11783 (2019).

42. M. M. Ruedaa, M-C. Auscher, R. Fulchiron, T. Périéc, G. Martin, P. Sonntag, P. Cassagnau, Rheology and applications of highly filled polymers: A review of current understanding. *Prog. Polym. Sci.* **66,** 22–53 (2017).

43. Y. Qiu, F. Guo, R. Hurt, I. Külaots, Explosive thermal reduction of graphene oxide-based materials: Mechanism and safety implications. *Carbon* **72**, 215–223 (2014).

44. D. Townsend, S. Parry, N. K. Bourne, P. J. Withers, D. C. Wood, G. J. Appleby-Thomas, A. Hameed, On the compression of aluminum foam structures under shock. *AIP Conf. Proc.* **1793**, 110010 (2017).

45. M. K. Zhang, P. J. Zhang, Q. Wang, L. Li, S. J. Dong, J. Liu, W. Rao, Stretchable liquid metal electromagnetic interference shielding coating materials with superior effectiveness. *J. Mater. Chem. C* **7**, 10331–10337 (2019).

46. F. Shahzad, M. Alhabeb, C. B. Hatter, B. Anasori, S. M. Hong, C. M. Koo, Y. Gogtosi, Electromagnetic interference shielding with 2D transition metal carbides (MXenes). *Science* 353, 1137–1140 (2016).

47. D. P. H. Hasselman, K. Y. Donaldson, J. Liu, L. J. Gauckler, P. D. Ownby, Thermal conductivity of a particulate-diamond-reinforced cordierite matrix composite. *J. Am. Ceram. Soc.* **77**, 1757–1760 (1994).

48. S.-H. Joo, D.-H. Pi, A. D. H. Setyawan, H. Kato, M. Janecek, Y. C. Kim, S. Lee, H. S. Kim, Work-hardening induced tensile ductility of bulk metallic glasses via high-pressure torsion. *Sci. Rep.* **5**, 9660 (2015).

49. J. N. Hohman, M. H. Kim, G. A. Wadsworth, H. R. Bednar, J. Jiang, M. A. LeThai, P. S. Weiss, Directing substrate morphology via self-assembly: Ligand-mediated scission of gallium-indium microspheres to the nanoscale. *Nano Lett.* **11**, 5104–5110 (2011).

50. C. V. Ramana, E. J. Rubio, C. D. Barraza, A. M. Gallardo, S. McPeak, S. Kotru, J. T. Grant, Chemical bonding, optical constants, and electrical resistivity of sputter-deposited gallium oxide thin films. *J. Appl. Phys.* **115**, 043508 (2014).

51. R. Al-Gaashani, A. Najjar, Y. Zakaria, S. Mansour, M. A. Atieh, XPS and structural studies of high quality graphene oxide and reduced graphene oxide prepared by different chemical oxidation methods. *Ceram. Int.* **45**, 14439–14448 (2019).

52. X. P. Shui, D. D. L. Chung, Nickel filament polymer-matrix composites with low surface impedance and high electromagnetic interference shielding effectiveness. *J. Electron. Mater.* **26**, 928–934 (1997).

53. H. Ji, R. Zhao, N. Zhang, C. X. Jin, X. F. Lu, C. Wang, Lightweight and flexible electrospun polymer nanofiber/metal nanoparticle hybrid membrane for high-performance electromagnetic interference shielding. *NPG ASIA Mater.* **10**, 749–760 (2018).

54. B. Shen, W. T. Zhai, W. G. Zheng, Ultrathin flexible graphene film: An excellent thermal conducting material with efficient EMI shielding. *Adv. Funct. Mater.* **24**, 4542–4548 (2014).

55. J. Ling, W. Zhai, W. Feng, B. Shen, J. Zhang, W. g. Zheng, Facile preparation of lightweight microcellular polyetherimide/graphene composite foams for electromagnetic interference shielding. *ACS Appl. Mater. Interfaces* **5**, 2677–2684 (2013).

56. B. Shen, Y. Li, W. T. Zhai, W. G. Zheng, Compressible graphene-coated polymer foams with ultralow density for adjustable electromagnetic interference (EMI) shielding. *ACS Appl. Mater. Interfaces* **8**, 8050–8057 (2016).

57. Y. Li, X. L. Pei, B. Shen, W. T. Zhai, L. H. Zhang, W. G. Zheng, Polyimide/graphene composite foam sheets with ultrahigh thermostability for electromagnetic interference shielding. *RSC Adv*. **5**, 24342–24351(2015).s